Experimental and Theoretical Investigation of Flow Generated by an Array of Porous Tubes

J.M. Avidor,* N.H. Kemp,† and C.J. Knight‡
Avco Everett Research Laboratory, Inc., Everett, Mass.

A novel scheme of introducing flow into an electric discharge laser (EDL) cavity has been developed and is described here. The flow, which is generated by a grid of parallel porous tubes, has been studied experimentally and theoretically. Detailed measurements of the flowfield structure using hot-wire anemometry have been carried out and some turbulence data obtained near the porous tubes. A theoretical model based on rotational inviscid flow near the porous tubes is developed. The vorticity distribution is chosen to satisfy both the mass flux and no slip conditions on the tube walls. The near field flow exhibits a wake downstream of the tubes. A vorticity diffusion model is introduced to render the flow uniform in the far field. Agreement is shown between experiment and theory.

Nomenclature

b = distance from the back wall to tube center
$2c$ = spacing between tube centers
L_f = longitudinal integral scale
p_0 = plenum pressure
R = porous tube radius
Re_t = $u_n R/\nu_t$ turbulent Reynolds number
$R(\tau)$ = velocity autocorrelation
u = velocity component in the x-direction
u' = rms velocity fluctuation
u_n = normal injection velocity
ω = vorticity
x = coordinate normal to the back wall
y = coordinate parallel to the back wall
z = coordinate along tube axis

I. Introduction

THE average output power of multiple-pulsed electric discharge laser devices depends not only on the per pulse energy out of the device but also on the flow in the cavity that serves to remove the processed laser gas out of the lasing region in the interval between pulses. Fast, efficient mass transport has been successfully achieved in a gas flow configuration transverse to both the optical axis and electric field[1] (Fig. 1a). However, there are cases in which it becomes desirable to flow the gas parallel to the electric field (Fig. 1b). To achieve the latter, a novel scheme based on generating a flow in a cavity by injecting gas through a grid of porous tubes has been developed here.

Recently, there have been some studies[2,3] that experimentally investigated the flow downstream of a jet grid placed in a uniform flow. The emphasis of those investigators was to highlight the jet grid effects on the far downstream ($x/2c<30$) turbulence. Although some aspects of that flow resemble the present porous tube grid flow far enough downstream of the array, here we are interested in the near field flow region ($x/2c<10$), which is strongly dependent on porous tube gas injection characteristics, tube spacing, wall position, and other parameters.

The experiments reported here were undertaken in order to understand the generation and near field of the flowfield downstream of a porous tube array. Specific objectives were to study the development of the flowfield with uniform mass injection along the porous tubes, in particular the effects of grid mesh size and wall-to-grid spacing. Also investigated, but not reported here, was the effect of introducing nonuniform circumferential velocity distribution around the porous tubes as a way of reducing flowfield nonunformities.

In conjunction with the experimental effort, a theoretical model based on rotational inviscid flow has been developed for the flow region very close to the porous tubes. To account for the decay of the wake-like near-field flow, a vorticity diffusion model is developed and applied. Using these models, overall good agreement between experiment and theory has been obtained.

II. Apparatus and Experimental Results

The porous tubes used in the present study were manufactured by Mott Metallurgical, Farmington, Conn. The tubes are fabricated from metallic powder (S.S. 316) to yield controlled porosity porous tubes. The powder is precompressed into a form by the application of a controlled pressure, and subsequently heated to the sintering temperature. The tubes used here averaged 0.25 in. in i.d. and 0.0625-in. wall thickness and were 13 in. long. The deviation in i.d. and wall thickness were 0.015 in. and 0.010 in., respectively.

Because of the longitudinal pressure drop inside the porous tube induced by the axial flow, the radial pressure drop through the tube wall itself was designed to be large in order that the radial mass injection rate be uniform along the tube length. To insure the latter, very low-porosity tubes were used here, designated by the manufacturer as having 0.5-μ filtration rating. With this rating, a pressure differential of 150 psi produced about a 7-m/sec mean radial velocity (at atmospheric pressure) at the outer tube surface. Results of hot-wire measurements along a tube, with an example presented in Fig. 2, show large amplitude fine-scale modulations in the radial flow velocity along the tube surface. However, the mean remains quite constant along the entire tube length.

The porous tubes were arranged in a parallel grid and connected to two large diameter pipes (2 in. i.d.). The use of two large diameter pipes allowed the possibility of having flow enter the tubes simultaneously from both ends. This option was not required, however, since no major change in injected mass flow was measured. The tubes were fed with high-pressure nitrogen through one side only, one pipe served as a flow-

---

Presented as Paper 76-59 at the AIAA 14th Aerospace Sciences Meeting, Washington D.C., Jan. 26-28, 1976, submitted Feb. 27, 1976; revision received Aug. 25, 1976. Work supported under ARPA Contract No. N0014-72-C-0276.

Index categories: Jets, Wakes, and Viscid-Inviscid Flow Interaction.

*Principal Research Scientist. Member AIAA.

†Principal Research Scientist, presently with Physical Sciences Inc., Woburn, Ma. Associate Fellow AIAA.

‡Principal Research Scientist. Member AIAA.

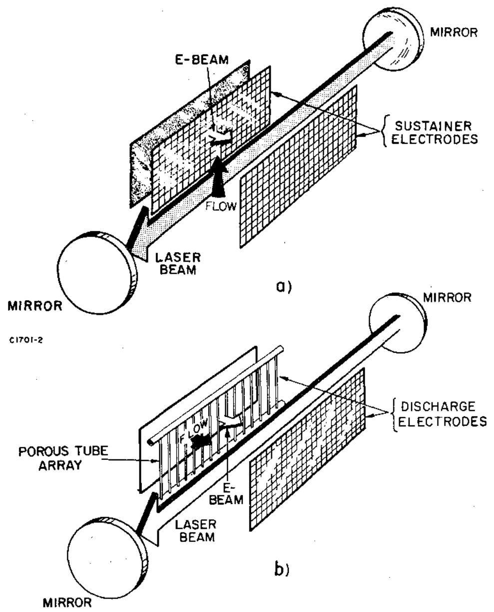

Fig. 1 Transverse and parallel cavity flow.

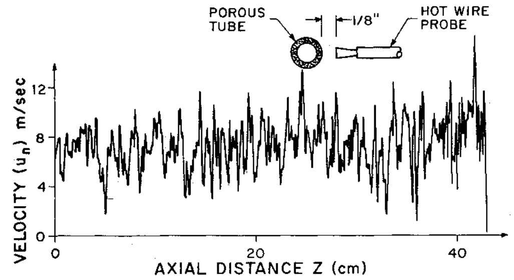

Fig. 2 Distribution of the normal injection velocity along a single porous tube.

source plenum chamber and the other as a dead-end connection. The parallel porous tube array (12×13 in. overall dimensions) was then enclosed in a 12-in.-high plexiglass enclosure to prevent entrainment of ambient air into the near field of the porous tube generated flow (Fig. 3).

Compressed nitrogen was supplied to the grid from a high-pressure bottle bank. The supply pressure was regulated using a dome pressure regulator, which ensured constant plenum pressure during each test run. No filtration of the gas was carried out, and as it turned out no degradation of the low-porosity tube flow capability was observed over a large number of tests.

Hot-wire anemometry was used here for mean flow velocity and rms velocity fluctuation measurements. The constant-temperature hot-wire system (Thermo Systems, Inc.) consisted of a constant temperature anemometer in conjunction with a linearizer yielding a linear net calibration curve. A true rms voltmeter served to obtain rms velocity fluctuations, and (in conjunction with an analog divider) yielded turbulence intensity data.

In the first set of experiments, the array was arranged with 13 porous tubes spaced 2.5 cm apart ($2c=2.5$ cm) and at a distance of 2.5 cm from the back wall. Holding the plenum pressure constant at $p_0=150$ psig the mean axial velocity distribution and the turbulent velocity fluctuations were measured at several downstream sections. The results presented in Fig. 4 show how the flowfield evolves from the porous tube surface to approximately eight tube spacings downstream of the grid. In general, the flow displays a wake-like behavior, with small variations present between the different wakes, presumably due to some nonuniformities in the injection through the different porous tubes. Very close to the tubes ($x=3.0$ cm) evidence of the injection velocity is noticeable; moving further downstream this velocity pattern disappears. The large velocity nonuniformities associated with the wake-like flow rapidly decay and at about $x/2c=9$ the mean flow is quite uniform. Looking at the turbulence intensity (u'/u) distribution at a typical location in the near field (at $x=5.0$ cm), the maximum value of turbulent velocity fluctuations seems to occur at the point of maximum shear, similar to behavior observed in turbulent jets and wakes; however, further downstream the peak intensity occurs at the center portion of the wake. The nonuniformities in the turbulence intensity also decay rapidly and a rather uniform distribution already exists at $x/2c=9$, with a turbulence intensity (u'/u) level of about 8%.

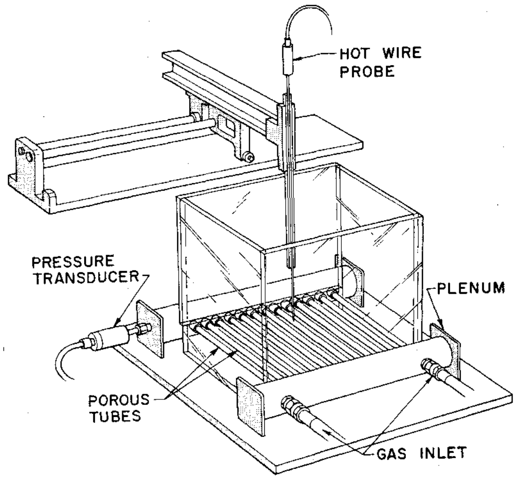

Fig. 3 Experimental setup.

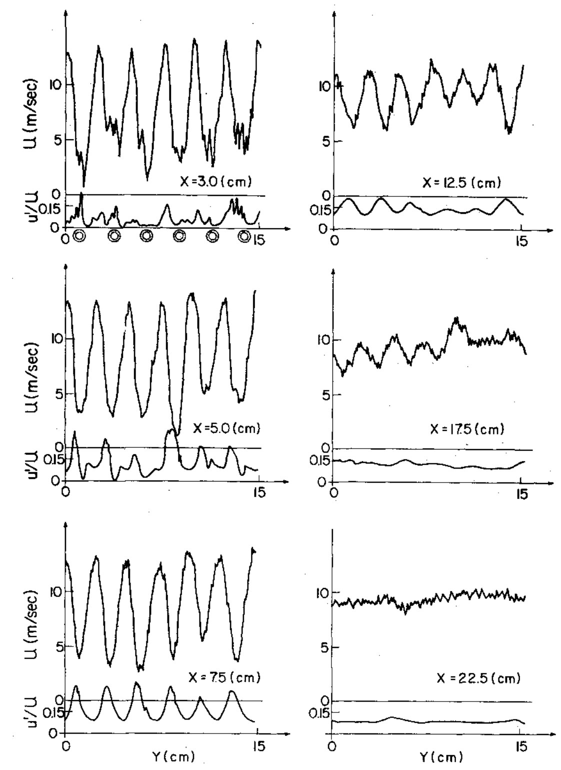

Fig. 4 Spatial development of the porous grid generated flow ($2c=2.5$ cm).

The results of increasing the porous tube spacing to 7.5 cm are presented in Fig. 5. For this wider spacing, increasing the plenum chamber to 350 psig produces the same mean flow

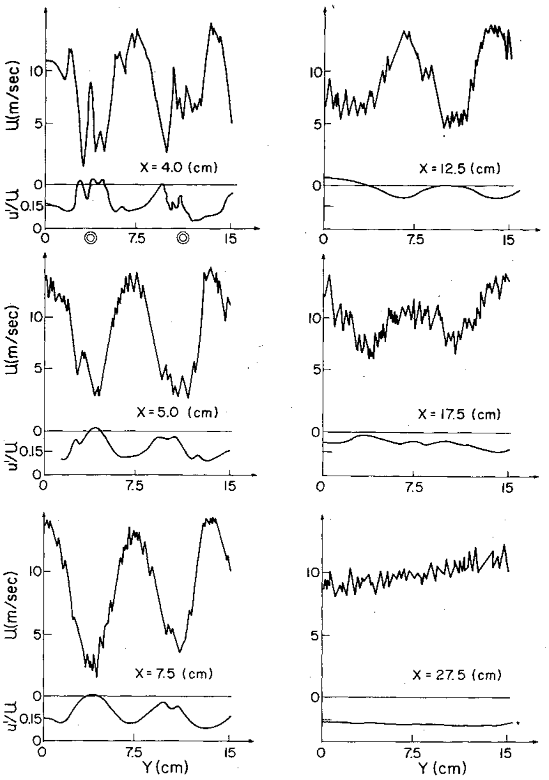

Fig. 5 Spatial development of the porous grid generated flow ($2c = 7.5$ cm).

velocity as in the previous test series (Fig. 4). This, however, resulted in a substantial increase in the injection velocity as one observes in the velocity scan taken at $x = 4.0$ cm, with the injection velocity pattern still noticeable at the $x = 7.5$ cm station. In general, as in the previous case, a wake-like flow evolves. However, a more rapid decay seems to occur, with a rather uniform flow attained at $x/2c \approx 3$. The increase in injection velocity also resulted in an overall increase in the turbulence intensity, which agrees with similar results reported by Tassa et al.,[3] who also observed an increase in turbulence intensity downstream of a jet grid with increasing injection rates through the grid. The increase in the turbulence intensity for the larger tube spacing is probably the reason for the more rapid velocity decay observed in this case.

Of interest also was the effect of the back wall position on the flowfield structure behind the grid. To study this effect the back wall in our investigation was positioned right against the tubes of the 2.5-cm and 7.5-cm grids. The results (not shown here) show that in the cases studied the back wall position has no discernible effect on the flow downstream of the grid, in terms of mean or fluctuating velocity level or distribution.

III. Theory

Source Model

A simple but tractable model of the flow generated by a row of porous tubes parallel to a wall can be obtained by representing the tubes by sources, as shown on the right side of Fig. 6. The wall is represented by a row of image sources on the left side of the figure.

The flowfield of this double row of sources is easily found in closed form, in terms of the source spacing $2c$, the distance from the wall, b, and the source strength (volume flow per unit depth and time) Q. The superimposed velocity fields of each row of sources can be summed as a hyperbolic contangent, and the complex velocity in terms of $z = x + iy$ becomes

$$u - iv = \frac{Q}{2c} \frac{\sinh(\pi z/c)}{\cosh(\pi z/c) - \cosh(\pi b/c)} \tag{1}$$

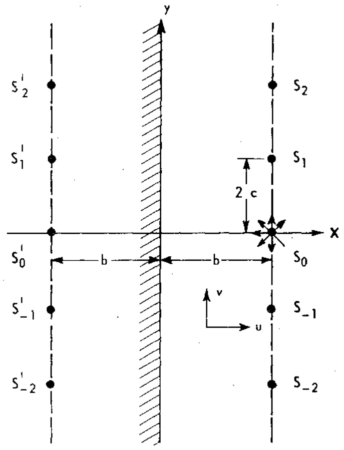

Fig. 6 Geometry of row of sources S_n, and image sources S_n' representing wall.

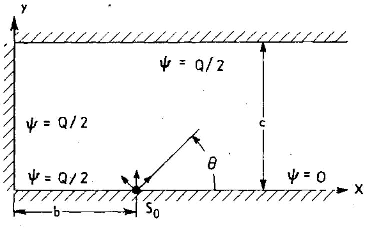

Fig. 7 Cell used for calculation of source model.

The symmetry and periodicity of this flow permits us to deal only with one cell covering the region $0 \le y \le c$, $x \ge 0$. The cell $c \le y \le 2c$ is the mirror image of this one in the line $y = c$, and the rest of the field is periodic in y with period $2c$. This basic cell is equivalent to one with walls on $x = 0$ and on $y = 0$, c, and a source at $x = b$, $y = 0$, as shown in Fig. 7.

The stream function Ψ may be chosen to have $\Psi = Q/2$ on the upper wall $y = c$, the left wall $x = 0$, and the part of the bottom wall $y = 0$ for which $0 < x < b$. Then the value of Ψ on the part of the bottom wall for which $x > b$ may be taken as $\Psi = 0$. Integration of the complex velocity Eq. (1) then gives Ψ as

$$\Psi = Q/2 \arctan\left[\frac{\sinh(\pi x/c)\sin(\pi y/c)}{d}\right] \tag{2}$$

$$d = \cosh(\pi x/c)\cos(\pi y/c) - \cosh(\pi b/c)$$

where the arc tangent is in the interval $(0, \pi/2)$ for positive argument and $(\pi/2, \pi)$ for negative argument.

The streamlines for the case $b/2c = 1$ are shown in the cell in Fig. 8, where the x,y scales are normalized with the length c and the source strength Q is taken as 2π. Each streamline is labeled with the fraction of π, i.e., the fraction of the flow between the wall and that streamline.

We see that the whole region between the source and the wall is filled with only a small fraction of the fluid. Half that space ($1 > x/c$) is filled with little more than 1/100 of the fluid emerging from the source, and the streamline enclosing 1/20 of the fluid never gets closer to the wall than $x/c > 1.4$. Thus the velocity of flow between the source and the wall is on the whole quite slow.

To the right of the source, away from the wall, the flow eventually becomes uniform with velocity $u = Q/2c$. The approach to this condition occurs exponentially in x, as seen from Eq. (1). In fact, for $b/2c = 1$, the u velocity varies with y across the cell only from 0.72 Q/c to 0.48 Q/c at $x = 3c$ (which is a distance $b/2$ from the source), and from 0.5009 Q/c to 0.485 Q/c at $x = 4c$ (which is a distance b from the source). Thus u becomes uniform very quickly, and its value at the level of the source ($y = 0$) is always larger than its value at a level half-way between the sources ($y = c$).

Although the source model is simple analytically, and gives useful information about the flowfield, it has several flaws.

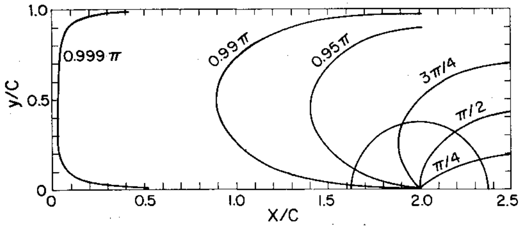

Fig. 8 Streamlines for the source model.

First, it takes the tubes as point sources and ignores the effect of their finite size on the flow. Second, it gives a nearly uniform flow only a short distance from the sources. What nonuniformity there is, is at variance with the experiments, which show slower flow directly over the tubes than half-way between them. The second property is common to any irrotational flowfield, which cannot lead to a significantly nonuniform flow profile well downstream of the tubes because that would imply vorticity.

Postulated Flow Structure

These observations led to the hypothesis that better agreement between theory and experiment would result if we supposed instead an inviscid rotational flowfield near the tubes. So long as viscosity effects can be ignored, the vorticity transport equation is simply

$$\left(\frac{\partial\psi}{\partial y}\frac{\partial}{\partial x}-\frac{\partial\psi}{\partial x}\frac{\partial}{\partial y}\right)\nabla^2\psi=0 \tag{3}$$

Since this equation is third order, it permits imposing two boundary conditions on the tube walls, where fluid comes into the region.

We actually deal in this paper with the following nonlinear Poisson equation which can be derived directly from Eq. (3).

$$\nabla^2=-\omega(\psi) \tag{4}$$

where ω is the vorticity. All the vorticity is brought into the flowfield on streamlines emanating from the cylinder, and the boundary conditions imposed there determine the functional dependence $\omega(\psi)$. We adopt the physically realistic requirement of zero tangential velocity at the tube surface and a specified normal velocity distribution.

To see that vorticity can lead to the experimentally determined velocity profiles far from the tubes note that all derivatives with respect to x approach zero rapidly as $x\rightarrow\infty$. Thus, Eq. (4) becomes $\psi_{yy}\sim-\omega(\psi)$ or

$$\psi_y\frac{\partial}{\partial\psi}(N_y)=\frac{\partial}{\partial\psi}\left[\frac{1}{2}\left(\frac{\partial\psi}{\partial y}\right)^3\right]\sim-\omega(\psi) \tag{5}$$

Since $\partial\psi/\partial y=u$, the velocity in the x-direction, integration with $u=u_0$ on $\psi=0$, the streamline at the level of the tube center, gives

$$u^2=u_0^2-2\int_0^{\psi}\omega(\eta)\,\mathrm{d}\eta \tag{6}$$

It is immediately evident that u will increase with ψ away from $\psi=0$, as observed experimentally, provided $\omega<0$. As we will show later, the no-slip condition imposed on the tube walls does lead to negative vorticity throughout the flowfield when the normal velocity at the tubes in uniform.

Of course, nonuniform vorticity cannot exist indefinitely downstream of the tubes because it is transported by diffusion, primarily due to turbulence in our case. Thus, we will generally need to match the inviscid solution constructed in the near field with a treatment of the far-field decay of the wake-like structure. Details of how this is done will be deferred until the end of this section.

Numerical Treatment of the Rotational Inviscid Near-Field

The numerical scheme used involves the following steps to solve the near-field flow problem:

1) Assume an initial vorticity distribution $\omega^{(0)}$, which in all our calculations is taken to be zero.

2) Solve the linear Poisson equation

$$\psi_{xx}^{(v)}+\psi_{yy}^{(v)}=-\omega^{(v)} \tag{7}$$

on the domain in Fig. 9 subject to the boundary conditions

$$\psi^{(v)}=0 \text{ on } y=0,\ b+1\leq x\leq x_\infty$$

$$\psi^{(v)}=\pi \text{ on } \begin{cases} y=0,\ 0\leq x\leq b-1 \\ x=0,\ 0\leq y\leq c \\ y=0,\ 0\leq x\leq x_\infty \end{cases}$$

$$\psi^{(v)}=\Theta \text{ on the circular arc segment} \tag{8}$$

$$\partial\psi^{(v)}/\partial x=0 \text{ on } x=x_\infty,\ 0\leq y\leq c$$

where v is the iteration number and Θ is the polar angle shown in Fig. 10. All variables are nondimensionalized using the normal velocity through the porous tube and the tube radius as reference scales.

3) Adjust the vorticity on the circular arc boundary such that the no-slip condition, $\partial\Psi/\partial r=0$, will be satisfied when the iteration converges $(v\rightarrow\infty)$.

4) Recompute vorticity values at all other grid points by interpolation of the revised vorticity distribution established in step 3. The values $\Psi^{(v)}$ are used in performing the interpolation.

5) Return to step 2 and continue the iteration until successive iterates show little change in vorticity distribution.

The procedure outlined above is motivated by work on solving the two-dimensional Navier-Stokes equations.[4-6] We had a choice of imposing Dirichlet or Neumann data on the circular arc boundary since both uniform normal velocity and no-slip are specified there. Direct enforcement of uniform normal velocity, as in Eq. (8), is preferred.

The technique used in step 2 is a finite-element method using nonuniform quadrilateral elements and a bilinear representation of ψ over the element in terms of skewed coordinates. Further discussion is given by Zienkiewics.[7] The resulting system of linear equations is solved by successive block overrelaxation as discussed by Cuthill and Varga.[8] The basic program incorporating this scheme was developed by Sackett.[9]

To derive the boundary vorticity adjustment scheme in step 3, rewrite Eq. (4) in a cylindrical coordinate system with origin at the tube center.

$$\frac{1}{r}\frac{\partial}{\partial r}\left(r\frac{\partial\psi}{\partial r}\right)+\frac{1}{r^2}\frac{\partial^2\psi}{\partial\Theta^2}=-\omega(\psi) \tag{9}$$

Since we are always maintaining $\psi=\Theta$ on the circular arc and we want to impose $\partial\psi/\partial r=0$ there, a reasonable estimate of the new boundary vorticity distribution follows from

$$\omega_B^{(v+1)}=-[\partial^2\psi^{(v)}/\partial r^2]_B \tag{10}$$

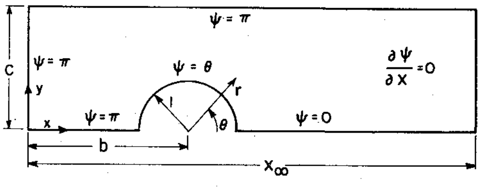

Fig. 9 Cell used for calculation of vortical model.

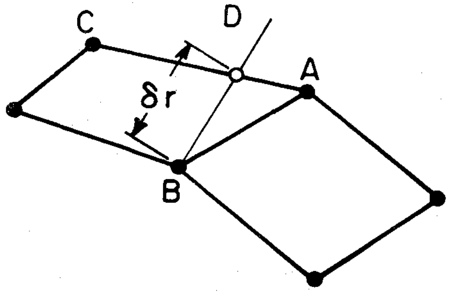

Fig. 10 Evaluation of radial derivative on the circular arc.

Note that if successive iterates on ω_B are the same, it must be true that the no-slip condition is satisfied.

Approximation of the second derivative in Eq. (10) can be accomplished in the following way with general quadrilateral finite elements shown in Fig. 10. Point B is on the circular arc and point D is the intersection of a radial line through B with a side on one of the adjacent quadrilateral elements. A Taylor series expansion about B gives

$$\psi_D = \psi_B + \frac{1}{2}\left(\frac{\partial^2\psi}{\partial r^2}\right)_B \delta r^2 + 0(\delta r^3) \tag{11}$$

where account has been taken of the requirement $(\partial\psi/\partial r)_B = 0$. Thus, a first-order approximation to Eq. (10) is

$$\omega_B^* = \frac{2}{\delta r^2}\left[\psi_B^{(\upsilon)} - \psi_D^{(\upsilon)}\right] \tag{12}$$

The values of $\psi_D^{(\upsilon)}$ is determined by linear interpolation between nodal values at the ends of the intersected line segment. For uniqueness, this line segment is restricted to be predominantly aligned with the boundary contour.

To improve convergence properties of the iteration scheme, Eq. (12) is taken only as an estimate of the boundary vorticity which is to be underrelaxed according to

$$\omega_B^{(\nu+1)} = \omega_B^{(\nu)} + \beta\left[\omega_B^* - \omega_B^{(\nu)}\right] \tag{13}$$

A typical value of β is 0.1. The value of $\omega_B^{(\upsilon+1)}$ is always required to be zero at $\Theta = 0$ and π, by symmetry, and the procedure embodied in Eqs. (12) and (13) is not applied at these points.

After step 3 we have new values of vorticity at each of the boundary nodal points, where the value of ψ is known from the polar angle according to Eq. (8). Using this information as data for an interpolation scheme (linear here), we then have a determination of the vorticity $\omega(\psi)$ on each streamline ψ = constant required in step 4. The vorticity is taken to be distributed over the field by the old streamlines.

Turbulent Vorticity Transport Model for the Far-Field Wake Decay

Since there will be a large velocity defect in the near wake, we cannot suppose the pressure is nearly uniform. To avoid consideration of this forcing function in the momentum equation, we will adopt the vorticity transport equation, in which pressure does not appear. Recognizing turbulent diffusion is predominantly transverse to the flow, we are led to consider

$$\begin{gathered}\frac{\partial^2\psi}{\partial x^2} + \frac{\partial^2\psi}{\partial y^2} = -\omega \\ \frac{\partial\psi}{\partial y}\frac{\partial\omega}{\partial x} - \frac{\partial\psi}{\partial x}\frac{\partial\omega}{\partial y} = \frac{\partial}{\partial y}\left(\upsilon_t\frac{\partial\omega}{\partial y}\right)\end{gathered} \tag{14}$$

where υ_t is the turbulent eddy viscosity.

To proceed, we will need to adopt an eddy viscosity model. Not too far downstream of the porous tubes, the velocity fluctuations are observed to be fairly uniform along a line parallel to the tube array. Also, the turbulence intensity decays slowly over distances of interest to us. On this basis it seems reasonable to try assuming a constant eddy viscosity. Note that in adopting this choice we have restricted attention to the region of the wake before self-similar flow is established. In the self-similar regime eddy viscosity is expected to decrease like x^{-1}.[2]

To be consistent with the remainder of the paper, we now introduce nondimensional variables

$$\tilde{\psi} = \psi/Ru_n,\ \tilde{\omega} = Rm/u_n,\ \tilde{x} = x/R,\ \tilde{y} = y/R \tag{15}$$

where R is the porous tube radius and u_n is the normal velocity through the tubes. Hopefully, it will cause no confusion if the tildas are now dropped, for notational simplicity, with the understanding that henceforth all variables are nondimensional. Then we can rewrite Eq. (14) as

$$\begin{gathered}\frac{\partial^2\psi}{\partial x^2} + \frac{\partial^2\psi}{\partial y^2} = -\omega \\ \frac{\partial\psi}{\partial y}\frac{\partial\omega}{\partial x} - \frac{\partial\psi}{\partial x}\frac{\partial\omega}{\partial y} = \frac{1}{Re_t}\frac{\partial^2\omega}{\partial y^2}\end{gathered} \tag{16}$$

where $Re_t = u_n R/\upsilon_t$ is an effective turbulent Reynolds number. The value of Re_t is to be determined by comparison with experimental results.

Variation of ω in the wake is over a y-scale of order one. The appropriate variable in the flow direction is $\tau = (x - x_0)/Re_t$, where $x = x_0$ is the virtual origin of the wake flow and is to be chosen. Restating the Poisson equation in Eq. (16) in terms of τ shows that the first term is of order Re_t^{-2}. Since the value of Re_t is expected to be at least 10, it is appropriate to neglect this first term in the subsequent analysis.

The treatment we adopt from this point employs ψ as the independent variable. Recalling Eqs. (5) and (6), the Poisson equation in Eq. (16) yields

$$u^2 = u_0^2 - 2\int_0^{\psi}\omega(\tau,\eta)\,\mathrm{d}\eta \tag{17}$$

and

$$y = \int_0^{\psi}\left[u_0^2 - 2\int_0^{\psi}\omega(\tau,\eta)\,\mathrm{d}\eta\right]^{-1/2}\mathrm{d}\psi \tag{18}$$

The value of u_0 follows by imposing mass conservation. That is, we require $y = c$ on $\psi = \pi$ to arrive at the transcendental equation

$$c = \int_0^{\pi}\left[u_0^2 - 2\int_0^{\psi}\omega(\tau,\eta)\,\mathrm{d}\eta\right]^{-1/2}\mathrm{d}\psi. \tag{19}$$

Evidently, the solution for u_0 is a function of τ.

In terms of the new independent variables, the vorticity transport equation is simply

$$\frac{\partial\omega}{\partial z} = \frac{\partial}{\partial n}\left(u\frac{\partial\omega}{\partial n}\right) \tag{20}$$

The initial data $\omega = \omega_0(\psi)$, taken to apply on $\tau = 0$, is provided by the near-field inviscid rotational flow model. Also, we have the boundary conditions $\omega = 0$ on $\psi = 0$, π required by symmetry.

The following steps are required to obtain the wake decay numerically according to the model just described: 1) Enter with a known distribution of ω on an equispaced ψ-grid covering the interval $(0,\pi)$. 2) Compute the value of u_0 by solving Eq. (19). 3) Compute the values of u and y for each ψ-

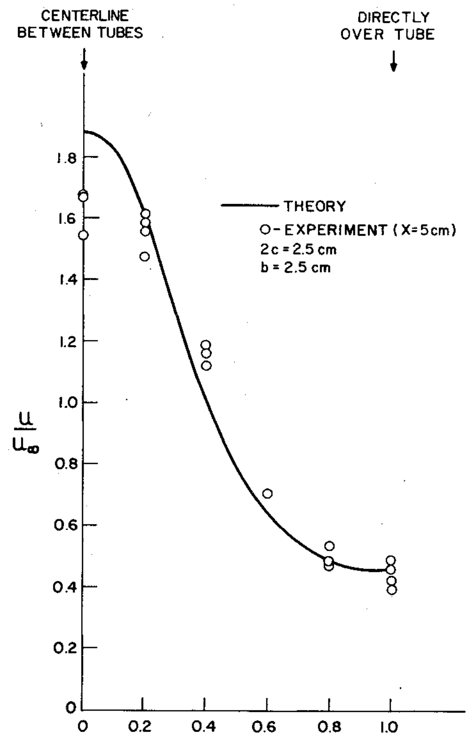

Fig. 11 Axial velocity distribution behind the grid ($2c = 2.5$ cm).

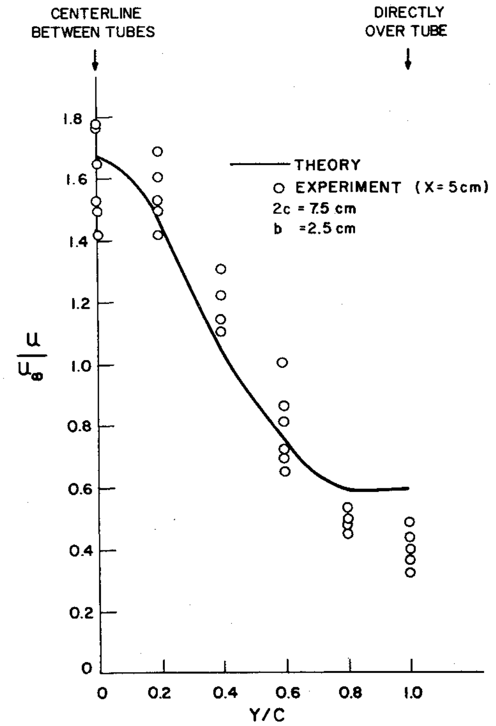

Fig. 12 Axial velocity distribution behind the grid ($2c = 7.5$ cm).

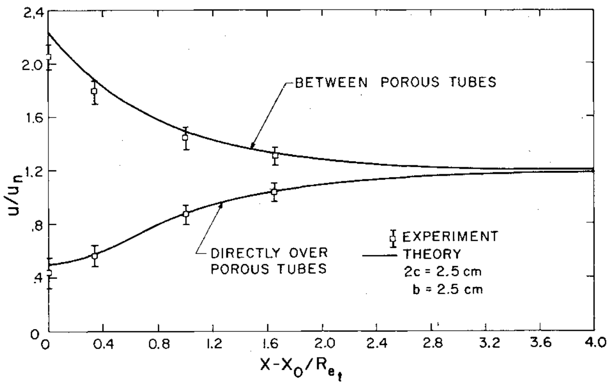

Fig. 13 Axial velocity decay ($2c = 2.5$ cm).

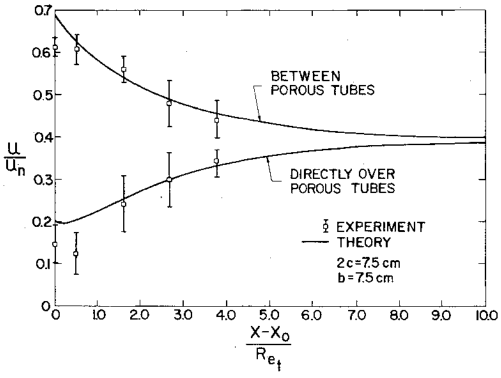

Fig. 14 Axial velocity decay ($2c = 7.5$ cm).

value according to Eq. (17) and (18) using trapezoidal rule integration. 4) Determine the ω distribution at the next τ-level from Eq. (20) by using an explicit difference scheme with ψ-derivatives evaluated by central differencing. 5) Repeat steps 1 to 4 until an adequate τ range is covered.

IV. Discussion

As has been observed, a wake-like flow is generated close to the porous tube grid, which rapidly decays to a uniform flowfield further downstream of the array. Using the rotational inviscid flow model developed in this study, numerical results have been obtained for cases investigated here and a comparison for two grid geometries is presented in Figs. 11 and Fig. 12. In general, good agreement is found between the experimental data and prediction in both cases presented. The experimental data indicates a flatter-than-predicted velocity distribuion in the interval between the tubes. Also noticeable is the larger scatter in experimental data for the larger-mesh-size grid. This increased scatter is attributed here to the increased injection velocity in this case in the following manner. For the purpose of comparison between experiment and prediction, data from a velocity distribution close to the grid ($x = 5.0$ cm) in which the wake-like flow structure is still present had to be used. However, due to the higher injection velocity, large differences between the wakes for each tube have been introduced as is evident in Fig. 5 as compared with Fig. 4, which resulted in larger scatter of the data.

Typical results for decay of maximum and minimum velocities in the wake toward the mean flow value are shown in Figs. 13 and 14 for two tube spacings. As has been pointed out in the analysis, the two parameters, turbulent Reynolds number Re_t and effective source position x_0, have to be determined by comparison with the experimental results for the purpose of comparing the experimental data with the predicted decay. The best fit shown in Fig. 13 for the smaller mesh grid has been obtained by setting $Re_t \approx 16$ and $x_0 = 5.0$ cm. The value for Re_t is similar to results obtained in other wake flow studies.[10] It was also found that the results are not very sensitive to the value chosen for x_0, which was set at 5.0 cm, since at this point downstream of the grid a rather clean wake-like flow has been established for this grid geometry. For the larger-mesh-size grid (Fig. 14), we maintained the same x_0 as before; however, the turbulent Reynolds number had to be decreased to $Re_t = 10$ so as to achieve the best fit between the experimental results and prediction. One can also see the large scatter in the data in this case, which again is a

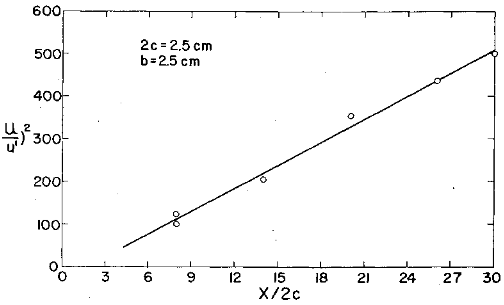

Fig. 15 Decay of turbulent energy ($2c = 2.5$ cm).

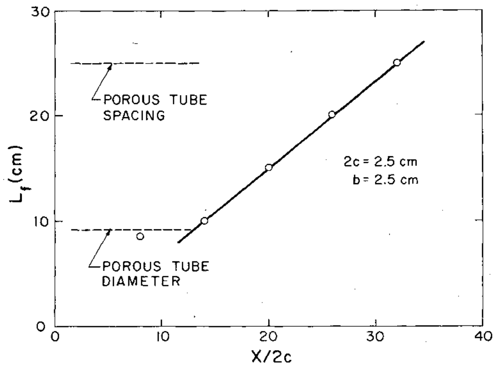

Fig. 16 Axial distribution of longitudinal scale size ($2c = 2.5$ cm).

result of the increased injection velocity for the larger-mesh-size grid.

It has been felt that the porous tube generated flow will possess typical grid flow characteristics, namely: isotropic turbulence far enough downstream of the grid. To verify the latter, two turbulence characteristics, the turbulence energy decay and integral scale size, were measured.

Decay of isotropic turbulence behind a grid can be described by the relation[11]

$$\left(\frac{u'}{u}\right)^2 = K\left(\frac{x}{2c} - \frac{x_0}{2c}\right)^{-n} \tag{21}$$

where x_0 is the location of the apparent origin of the decay, and K and n are constants. If the turbulence behind the present grid with injection is isotropic, it is expected to decay according to Eq. (21).

The results of the turbulent energy decay measurements for the 2.5-cm-mesh porous tube grid are presented in Fig. 15. As can be seen in the range of the measurements, from eight to approximately 30 tube spacings behind the grid, a linear decay is present. The best fit of the data was obtained with $x_0 = 0$, and the value for n was found to be 1.1, which is similar to results obtained by Tassa[3] and Gad-El-Hak.[2]

Invoking Taylor's hypothesis of frozen convection, the longitudinal integral scale, L_f, was computed from measured velocity autocorrelations and the mean flow velocity using the following relation

$$L_f = u\int_0^\infty R(\tau)\,d\tau \tag{22}$$

The results presented in Fig. 16 show how the integral scale size evolves from a size equivalent to the porous tubes diameter $2R = 0.93$ cm and $L_f = 0.86$ cm at $x/2c = 8$, to a scale similar to the tube spacing at $x/2c = 30$. A linear increase of the integral scale starting at $x/2c = 14$ is observed.

V. Conclusions

The following conclusions can be drawn regarding the porous tube generated flow. 1) a Wake-like flowfield is present behind the porous tube grid, which rapidly decays to a uniform flow. 2) The turbulence intensity of the flow increases with increasing injection velocity through the porous tubes. 3) Good agreement exists between experimental data and prediction by the rotational inviscid flow model of the near-field velocity distribution. 4) Rapid decay of velocity nonuniformities have been observed and reasonable agreement was found to exist with predictions based on the turbulent vorticity transport model. 5) Far downstream measurements of the porous grid generated flow properties indicate the presence of isotropic grid turbulence.

References

[1] Reilly, J.P., Avidor, J.M., Feinberg, R.M., and Theophanis, G.A., "Optimization of Sonic Jet Array Flow for Subsonic Electric Laser Medium Homogeneity," AIAA paper 75-849, Hartford, Conn., 1973.

[2] Gad-El-Hak, M. and Corrsin, S., "Measurements of Nearly Isotropic Turbulence Behind a Uniform Jet Grid," *Journal of Fluid Mechanics*, Vol. 62, Jan. 1974, pp. 115-143.

[3] Tassa, Y. and Kamotani, Y., "Experiments on Turbulence Behind a Grid with Jet Injection in Downstream and Upstream Direction," *Physics of Fluids*, Vol. 18, April 1975, pp. 411-414.

[4] Roache, P.J., *Computational Fluid Dynamics*, Hermosa, Albuquerque, New Mex., 1972, Chap II. C.

[5] Israeli, M., "A Fast Implicit Numerical Method for Time Dependent Viscous Flows," *Studies in Applied Mathematics*, Vol. 49, 1970, MIT Press, Cambridge, Mass., pp. 327-349.

[6] Knight, C.J., "Numerical Studies of Natural Convection in an Enclosure," Home Fire Project Rept., Harvard University, to be published.

[7] Zienkiewics, O.C. and Cheung, Y.K., *The Finite Element Method in Structural and Continuum Mechanics*, McGraw-Hill, New York, 1967, Chap. 5.

[8] Cuthill, E.H. and Varga, R.S., "A Method of Normalized Block Iteration," *Journal of the Association for Computing Machinery*, Vol. 6, No. 2, April 1959, pp. 236-244.

[9] Sackett, S.J. Lawrence Berkeley Lab. Rept. No. 1778, Berkeley, Calif., 1974.

[10] Townsend, A.A., *The Structure of Turbulent Shear Flow*, Cambridge University Press, Cambridge, Great Britain, 1956, p. 128.

[11] Batchelor, G.K., *The Theory of Homogeneous Turbulence*, Cambridge University Press, Cambridge, Great Britain, 1970, p. 137.